Cone Structure Persists Beyond Margins of Short-Wavelength Autofluorescence in Choroideremia

Katharina G. Foote,[1,2] Nicholas Rinella,[2] Janette Tang,[2] Nicolas Bensaid,[3] Hao Zhou,[4] Qinqin Zhang,[4] Ruikang K. Wang,[4] Travis C. Porco,[2,5] Austin Roorda,[1] and Jacque L. Duncan[2]

[1]School of Optometry and Vision Science Graduate Group, University of California, Berkeley, Berkeley, California, United States
[2]Department of Ophthalmology, University of California, San Francisco, San Francisco, California, United States
[3]Carl Zeiss Meditec AG, Berlin, Berlin, Germany
[4]Department of Bioengineering, University of Washington, Seattle, Seattle, Washington, United States
[5]Francis I. Proctor Foundation, Department of Ophthalmology, University of California, San Francisco, San Francisco, California, United States

Correspondence: Jacque L. Duncan, Department of Ophthalmology, University of California, San Francisco, 10 Koret Way, K113, San Francisco, CA 94143-0730, USA; Jacque.duncan@ucsf.edu.

Submitted: July 11, 2019
Accepted: October 7, 2019

Citation: Foote KG, Rinella N, Tang J, et al. Cone structure persists beyond margins of short-wavelength autofluorescence in choroideremia. *Invest Ophthalmol Vis Sci*. 2019;60:4931–4942. https://doi.org/10.1167/iovs.19-27979

Purpose. We studied the relationship between structure and function of the choriocapillaris (CC), retinal pigment epithelium (RPE), and photoreceptors in patients with choroideremia (CHM).

Methods. Six CHM patients (12 eyes) and four normal subjects (six eyes) were studied with fundus-guided microperimetry, confocal and nonconfocal adaptive optics scanning laser ophthalmoscopy (AOSLO), near-infrared and color fundus photos, short wavelength fundus autofluorescence (SW-AF), and swept-source optical coherence tomography (SS-OCT) and angiography (SS-OCTA) images. Cone spacing was represented using Z-scores (standard deviations from the mean at that eccentricity). CC flow voids were defined using a threshold of 1 SD below the normal mean.

Results. Cone spacing Z-scores were not significantly correlated with distance from the borders of preserved RPE, determined using either the SS-OCT or SW-AF scans. Cone spacing Z-scores were significantly correlated with CC flow voids and retinal sensitivity. Flow voids were abnormal in regions of preserved RPE and increased progressively from within $-2°$ of the preserved area to $+2°$ beyond the border. Visual sensitivity decreased as CC flow voids increased approaching and beyond the border of preserved structure.

Conclusions. In CHM, cone spacing Z-scores correlated with CC flow voids, and were negatively correlated with retinal sensitivity, suggesting cone degeneration accompanied reduced CC perfusion. Functional cones were found outside the presumed borders of preserved outer-retina/RPE as defined by SW-AF, but not outside the borders determined by SS-OCT. The use of SW-AF to identify the border of preserved structures may underestimate regions with cells that may be amenable to treatment.

Keywords: choroideremia, fundus autofluorescence, microperimetry, adaptive optics scanning laser ophthalmoscopy, optical coherence tomography angiography

Choroideremia (CHM) is an X-linked inherited degenerative disease estimated to affect 1:50,000 persons and is caused by a mutation in the *CHM* (*REP1*) gene on chromosome Xq21.[1] Patients suffer progressive loss of night vision, peripheral visual field loss, and eventual central vision loss. Although the pathogenic mechanism underlying degeneration in CHM is not clearly understood, it may be due to reduced function of proteins that have a role in organelle formation and vesicle trafficking.[2]

CHM leads to degeneration of the choriocapillaris (CC), retinal pigment epithelium (RPE), and photoreceptors, but the temporal relationship in which different cell types are affected remains unclear. Studies of induced pluripotent stem cells derived from CHM patients and differentiated into RPE cells demonstrate abnormal trafficking of melanosome granules to the apical surface and abnormal phagocytosis, which may cause photoreceptor degeneration.[3] However, RPE cells studied in isolation may not accurately reflect cellular function in vivo.

The lack of animal models of CHM makes clinical characterization of CHM patients especially valuable, and advances in technology to measure structure and function of photoreceptors, RPE, and CC in human eyes is making this increasingly possible.[1,4,5] The following sections outline some of the current methods used to assess structure and function in CHM and summarize the main findings from previously published results.

Photoreceptor Imaging

B-scans from conventional spectral domain optical coherence tomography (SD-OCT) or swept-source OCT (SS-OCT) can be used to measure the average length of photoreceptor inner segments (IS) and outer segments (OS).[6–12] Adaptive optics (AO) is a set of optical techniques that can measure and correct aberrations that cause blur of retinal images.[13] It can be integrated into any type of ophthalmic optical imaging modality (OCT),[14]

scanning laser ophthalmoscopy (SLO),[15] or fundus camera[13] to increase resolution to a level where individual cells can be resolved. AO systems enable the measurement of photoreceptor spacing and/or density in living humans.[16] AOSLO can be used in confocal mode to visualize the photoreceptor mosaic by direct backscatter from waveguiding photoreceptors. More recently, phase contrast techniques have been implemented into AOSLO to reveal multiple scattering and index of refraction changes.[17,18] Specifically, split-detector AOSLO systems have proven to be effective at revealing cone ISs in human retinal images outside of the fovea and revealing borders of lesions in CHM.[19,20] Finally, photoreceptor function can be tested at targeted locations using fundus-guided microperimetry.[20–22]

RPE Imaging

OCT is effective at visualizing the RPE monolayer.[23,24] The RPE signal in OCT is presumed to originate from backscattered light from RPE melanin.[25] En face visualizations of the RPE can be made by SS-OCT images that use 1050 nm light to provide deeper penetration for improved visualization of the RPE and CC[26–28] and to offer higher contrast measurements of RPE coverage. Another way to visualize the RPE is through fundus autofluorescence, which has been used to measure regions of intact RPE in patients with CHM.[29] Short wavelength autofluorescence (SW-AF) signals from bisretinoid constituents are naturally exhibited by photoreceptor OS and RPE cells when excited by an external light source.[30] When lipofuscin formation is increased due to disease, excess lipofuscin accumulates in RPE cells, which appear as hyperfluorescent areas in AF images.[31] The most effective modality for SW-AF autofluorescent imaging is the SLO, which uses confocal optical sectioning to reduce noise from structures other than the RPE that may contain fluorophores.[32] Near-infrared autofluorescence (NIR-AF), also commonly imaged with an SLO, uses a 787 nm laser diode for excitation. In this modality, the fluorescence most likely originates from RPE melanin pigment.[29,33] NIR-AF imaging is more comfortable for patients and may pose less risk of RPE damage than SW-AF.[34,35] NIR-reflectance (NIR-REF) imaging has been shown to be strongly correlated with NIR-AF imaging and uses wavelengths similar to the light used to acquire infrared fundus images during OCT scans, which suggests that the sources of signals from OCT images may be similar to the sources of NIR-REF and NIR-AF images.[33,36] The RPE imaging methods described above measure either fluorophores or melanin coverage and use that as a surrogate for RPE coverage. In conditions like CHM, modality-dependent differences in the locations of the borders of preserved RPE have been reported,[36] and this has profound implications for studies of disease progression and etiology.

CC Imaging

OCT angiography (OCTA) is an emerging imaging modality that can reveal perfused vessels by virtue of the movement of blood cells.[37,38] In the best cases, OCTA can visualize the entire network of retinal vessels and capillaries and is moving toward achieving the same resolution in the CC and choroidal vasculature. Although the ability to measure flow remains limited, OCTA techniques can be used to measure vascular coverage. In the CC, the coverage of the CC is quantified as the percent of flow voids,[28] or percentage of area that is not perfused by the CC network. An increase in flow void may indicate reduced perfusion or loss of CC.

Main Findings in CHM

Multimodal approaches using two or more of the aforementioned techniques have proven to be very effective in analyzing structure and function of the photoreceptors, RPE, and CC, which are the key structures affected in CHM.[4,19] However, the primary source of degeneration remains unclear and results are conflicting. Some conflicts arise from discrepancies in the way the area of preserved RPE and/or vision is measured. Recent publications have reported differences in NIR-AF with SW-AF images in other inherited retinal degenerations, including Stargardt disease and CHM patients.[36,39] NIR-AF images demonstrate larger areas of RPE atrophy and correlate more closely with the ellipsoid zone (EZ) extent than SW-AF images in Stargardt disease patients.[39] Another study showed that cones (as identified by the visualization of the EZ band in OCT images) persisted beyond the preserved region of RPE as quantified through SW-AF.[40] Structural studies using various combinations of SD-OCT, confocal and nonconfocal split-detector AOSLO, OCT angiography (OCTA) imaging, and SW-AF[19,41–43] suggest that RPE cells are the primary site of degeneration and that the CC does not degenerate independently of RPE loss.[43] Functional studies using OCT and psychophysical tests have demonstrated loss of photoreceptor function first, perhaps independently or in conjunction with RPE depigmentation.[1,44,45]

To date, few reports have compared retinal function with structure using high-resolution retinal imaging approaches in CHM patients.[20] To clarify the relationship between outer retinal structure and function and extend prior studies,[19,20] we compared multimodal high-resolution studies of photoreceptor, RPE, and CC structure with photoreceptor function in patients with CHM.

Methods

Study Design

Research procedures followed the tenets of the Declaration of Helsinki. Voluntary informed consent was obtained from all subjects. The study protocol was approved by the institutional review boards of the University of California, San Francisco and the University of California, Berkeley.

Subjects

Twelve eyes of six CHM patients (average age, 37 ± 19.2 years) and six eyes of four healthy subjects with normal eye examinations (average age, 33 ± 11.6 years) were studied. There was no significant difference in ages of patients and normal subjects (*t*-test, $P = 0.35$; Table). The patients and subjects were from unrelated families, except for patients 30025 and 10040, who were father and daughter,[5] respectively. Patient 30025 was excluded from the cone spacing analyses due to poor image quality and retinal sensitivity analyses because the patient could not see the fixation target to perform microperimetry reliably. Five patients were male, and one (patient 10040) was a symptomatic carrier female with 100% X-inactivation, described previously.[5] Normal control subjects had no evidence of retinal degeneration on complete eye examination or fundus images and did not undergo genetic testing. Patients were excluded from the study if they had conditions that would affect imaging including nystagmus, cataract, and macular edema. Genetic testing was performed on patients through the Carver Nonprofit Genetic Testing Laboratory on a fee-for-service basis (40135), the eyeGENE research consortium[46–49] (10040, 30025, 40028, 40166) or using a next-generation sequencing panel through the My Retina Tracker registry genetic testing study (NCT 02435940; retinal dystrophy panel of 181 genes, Blueprint Genetics, Seattle, WA, USA; 40147).

Investigative Ophthalmology & Visual Science

Table. Clinical Characteristics

ID	Sex	Age	Diagnosis/Mutation	Eye	BCVA	Refractive Error
10040	F	36	*CHM* c.49+1G>A, splice site mutation, exon 1	OD	20/25	−2.00
				OS	20/25	−2.95
30025	M	75	*CHM* c.49+1G>A, splice site mutation, exon 1	OD	20/80	−1.50 + 0.25 × 180
				OS	20/80	−2.00 + 0.25 × 180
40028	M	22	*CHM* c.316 C>T, p.Gln106Stop	OD	20/25	−2.25 + 1.75 × 180
				OS	20/25	−1.25 + 1.50 × 170
40135	M	45	*CHM* IVS2+1G>A, aberrant mRNA splicing	OD	20/30	−3.25
				OS	20/30	−3.25
40147	M	26	*CHM* c.1770+2T>A, splice donor variant	OD	20/25	−1.00 + .025 × 005
				OS	20/20	−1.50 + 025 × 160
40166	M	18	*CHM* c.715 C>T, p.Arg239Stop	OD	20/32	−6.00 + 4.00 × 095
				OS	20/32	−6.00 + 4.00 × 080
10003	M	52	Normal	OS	20/16	0.00 + 050 × 180
40104	M	26	Normal	OD	20/16	plano
				OS	20/16	plano
40154	F	22	Normal	OD	20/16	+2.50
				OS	20/20	+1.50 + 0.05 × 152
40179	F	31	Normal	OD	20/20	+0.25 + 1.00 × 20

CHM, choroideremia; F, female; M, male; BCVA, best corrected visual acuity; OD, right eye; OS, left eye.

Fundus-Guided Microperimetry

Fundus-guided microperimetry using Macular Integrity Assessment software (MAIA, Centervue, Inc., Fremont, CA, USA) was used in this study to analyze macular sensitivity of patients with CHM. This instrument uses SLO with real-time fundus tracking at a rate of 25 frames/second using fundus landmarks as a reference for perimetry. The MAIA tracks the retina using near infrared (850 nm) SLO movies with 1024 × 1024 pixel sampling resolution over a 36° × 36° field of view. Goldmann III (26 arcmin, 0.43°) stimuli were presented at targeted locations for 200 ms on a 1.27 cd/m^2 background with a dynamic range of 36 dB.[50,51] A standard 4-2 strategy with a custom grid pattern extending every 1° from the central fixation out to 10° in the four cardinal directions was used. In addition, the grid pattern covered every 1° within the central 6°.

Confocal and Split-Detector AOSLO

We used a simultaneous confocal and nonconfocal split-detector imaging AOSLO system. Confocal imaging is an in vivo, noninvasive technique that records light emerging from the cone waveguide, comprised of scattered light from the IS/OS junction and the posterior tip of the OS.[52] Nonconfocal split-detector AOSLO[18] uses a reflective mask with an annulus in the image plane in place of a regular pinhole typically used for confocal detection. This method allows the confocal signal to be reflected into one detector, and then directs the multiply scattered, nonconfocal light from opposing sides of the annular aperture into two separate detectors. The split-detector signal is calculated as the difference between the two nonconfocal detectors divided by their sum.[18] Nonconfocal split-detector AOSLO is a type of phase-contrast imaging and can be especially useful in distinguishing areas where cone IS remain but OS are not waveguiding.[18] The AOSLO system used a mirror-based optical design,[53] and a deformable mirror with a continuous membrane surface and shaped with 97 actuators (DM97, ALPAO, Montbonnot-Saint-Martin, France). The system used 840 nm light for imaging and 940 nm light for wavefront sensing, and both sources were drawn from the same broadband supercontinuum source (SuperK EXTREME, NKT Photonics, Birkerod, Denmark) using a custom-built fiber coupler. 512 × 512 pixel videos were recorded over a 1.2° × 1.2° square field.

Cone Spacing

Montages of AOSLO images were created as described previously[16] and with automontaging software.[54] To identify the preferred retinal locus (PRL), a 10-second video was recorded as the patient observed a small circular fixation target delivered through modulation of the AOSLO scanning raster, whose location was recorded in the AOSLO video.[55] The PRL was used to define the foveal center for measures of eccentricity. Cone spacing measures were quantified using a density recovery profile method[56] as described previously.[16] This method was chosen to estimate cone spacing, since it allows for reliable estimates of cone spacing in mosaics where not all cones are clearly visible, and where cones are not closely packed into a hexagonal array. While other measures of cone spacing exist (like nearest neighbor distance or row-to-row spacing),[57] we chose to use cone spacing as a conservative measure of cone preservation, albeit perhaps a less sensitive measure of cone loss. Cone spacing was measured by two independent graders within a standardized 0.1°^{2} (42 × 42 pixel) box as described previously.[58] Cone spacing measures were made in regions with the clearest cone images that were as close as possible to the retinal locations where functional measures were acquired using the MAIA microperimetry, which were manually superimposed on AOSLO images. Average intraclass correlation coefficient (ICC) value for patients and normal subjects between the two graders was 0.91. Because cone spacing varies predictably with eccentricity from the fovea,[59,60] Z-scores, or the number of standard deviations from the normal mean at the eccentricity where the cone spacing was measured, were used to describe cone spacing and control for the effect of eccentricity on cone spacing measures.

Fundus Autofluorescence (FAF)

SW-AF images were acquired using in vivo confocal scanning laser ophthalmoscopy (SLO; Spectralis HRA+OCT; Heidelberg Engineering, Vista, CA, USA) with 488 nm excitation and a 500 nm barrier filter to block reflected light and permit autofluorescent light from the fundus to pass through.[31] Hyperfluorescent areas representing presumed areas of preserved RPE

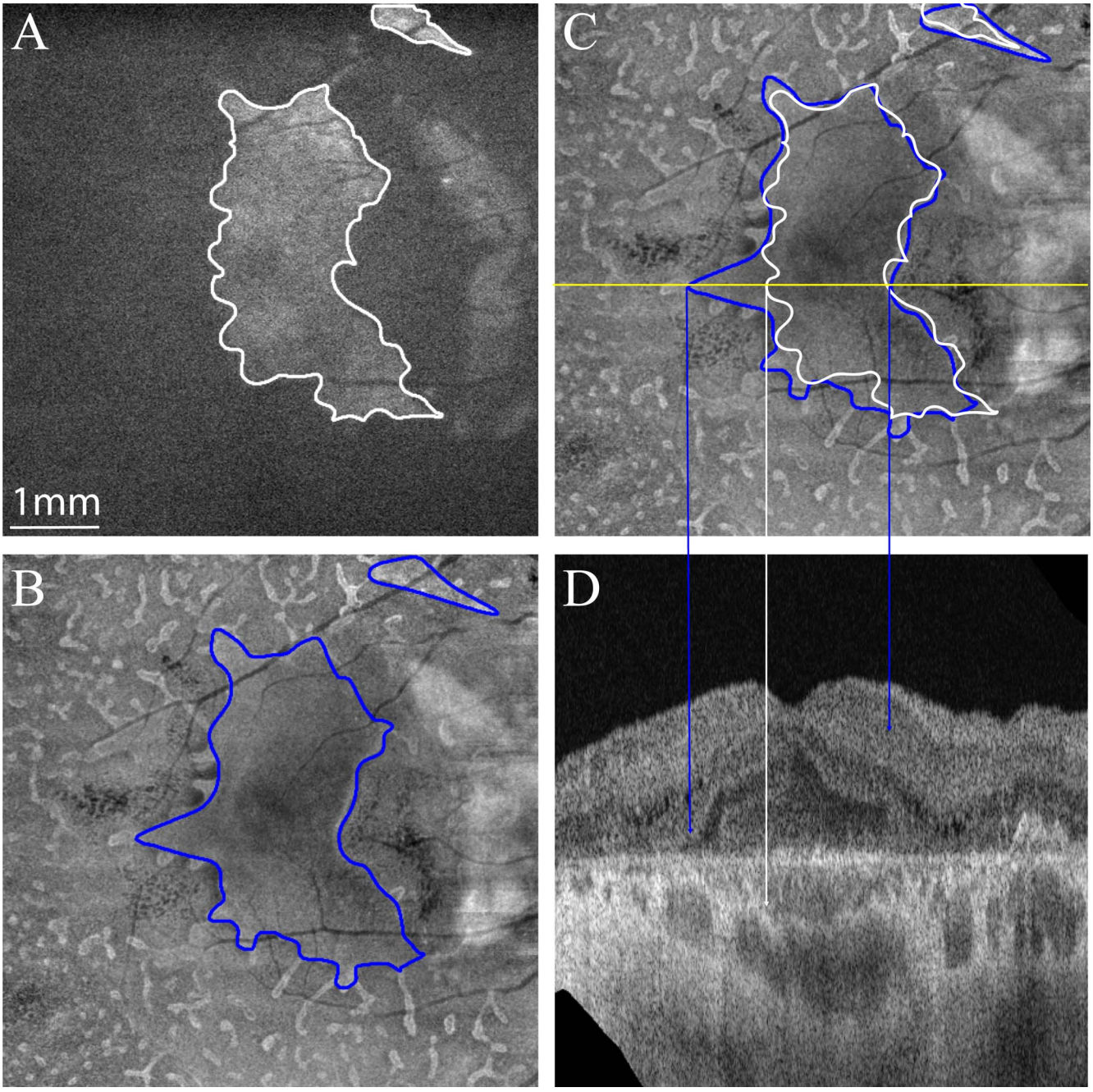

Figure 1. Borders of presumed area of preserved RPE based on SW-AF and SS-OCT in the right eye of patient 40028. (**A**) SW-AF image showing the SW-AF border manually outlined in *white*; (**B**) SS-OCT en face image of outer retina-RPE-CC slab extending from just below the outer plexiform layer to 8 µm beneath Bruch's membrane showing the SS-OCT border outlined in *blue*; (**C**) Borders from (**A**) and (**B**) superimposed; the *yellow horizontal line* shows the area from which the B-scan shown in (**D**) is taken, *white vertical lines* are projections of the SW-AF border while *vertical blue lines* are projections of the SS-OCT border; (**D**) B-scan that corresponds to en face image in (**C**). *Scale bar*: 1 mm (as estimated by PLEX Elite 9000, Carl Zeiss Meditec, Inc.).

cells on SW-AF images were manually outlined using Photoshop CC (Adobe, San Jose, CA, USA). Hereafter, the border of presumed regions of preserved RPE based on SW-AF images will be referred as the SW-AF border.[27,28]

SS-OCT and SS-OCTA

A SS-OCT (PLEX Elite 9000, Carl Zeiss Meditec, Inc., Dublin, CA, USA)[61,62] was used to visualize and semiautomatically identify presumed borders of preserved RPE. The SS-OCT has a swept source tunable laser centered between 1040 and 1060 nm, which records 100,000 A-scans/second with an optical axial resolution of 6.3 µm.[61,62] The borders were visualized using en face slabs that extended from just below the outer plexiform layer (outer retina) to 8 µm beneath Bruch's membrane.[27] Hereafter, the border of presumed regions of preserved RPE based on SS-OCT images will be referred as the SS-OCT border.

Figure 1 shows a comparison of the SW-AF and SS-OCT borders, which highlights differences in the borders of presumed preserved RPE depending on the method used.

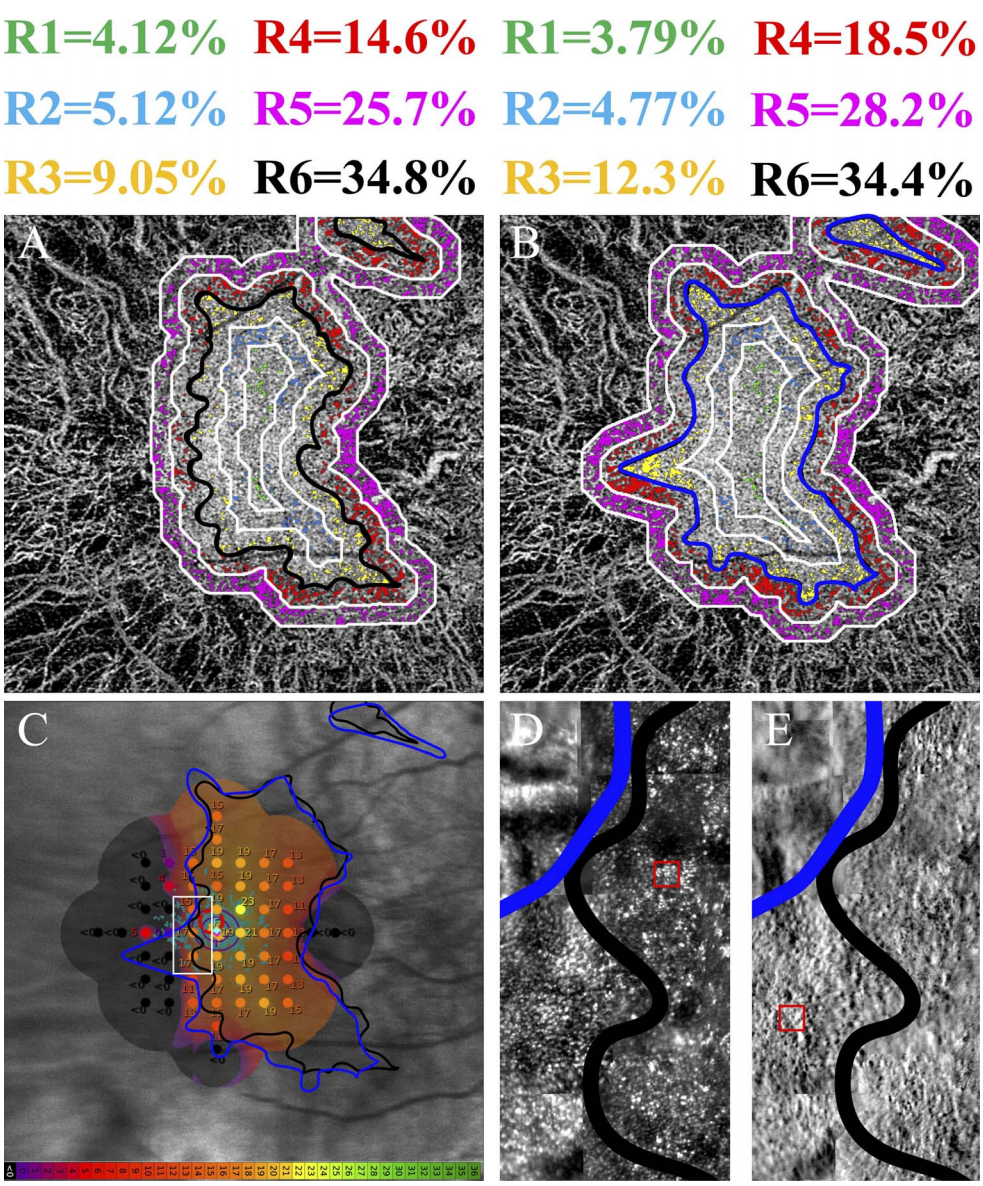

Figure 2. Multimodal images of structure and function from the right eye of patient 40028 show cones beyond the border of presumed RPE as defined by SW-AF border. (**A**) SS-OCTA CC slab with %FV shown in regions R1-R6 with SW-AF border outlined in *black*; (**B**) SS-OCTA CC slab with % FV shown in regions R1-R6 with SS-OCT border outlined in *blue*; (**C**) fundus-guided microperimetry retinal sensitivity image with SW-AF border in *black* and SS-OCT border in *blue*; the *color coded bar* shows the dynamic range, *white box* represents area in (**D**) and (**E**); (**D**) Confocal AOSLO image shows cone OSs with *blue* SS-OCT and *black* SW-AF borders superimposed; (**E**) Split detector AOSLO image shows cone ISs, same lines superimposed as in (**D**). For (**D**) and (**E**), *red boxes* indicate select regions of interest (ROIs) where cone spacing is measured. *Scale bar*: For (**A–C**): 1 mm (as estimated by PLEX Elite 9000, Carl Zeiss Meditec, Inc.).

SS-OCTA was used to visualize the CC in vivo from an en face slab extending from just below Bruch's membrane to 20 µm beneath Bruch's membrane.[27] CC perfusion was quantified as flow voids (FV), defined as a percentage of the imaged region representing CC flow with a reduction of pixel intensity of at least 1 SD below the mean CC flow. Mean CC flow was based on a normative database of 20 normal subjects aged 20 to 39 years.[27]

In Figures 2A and 2B, the black and blue contours represent the SW-AF and SS-OCT borders, respectively and the white contours indicate regions at 1° and 2° inside and outside the borders. In the innermost region R1 (delimited by the white contour 2° inside the border) the flow void pixels are colored green; in the outermost region R6 (outside the outer white contour), the flow void pixels are colored black. In the other regions R2-R5 delimited by the white contours and black border, the flow void pixels are colored in blue, yellow, red, and purple, respectively.

Statistical Methods

Descriptive statistics were calculated with means and SDs. Spearman correlation coefficients were calculated, with 95% confidence intervals (CIs) derived from bootstrap resampling at the patient level.

Results

Histologic studies have demonstrated a strong relationship between eccentricity from the fovea and cone spacing.[59,60] In

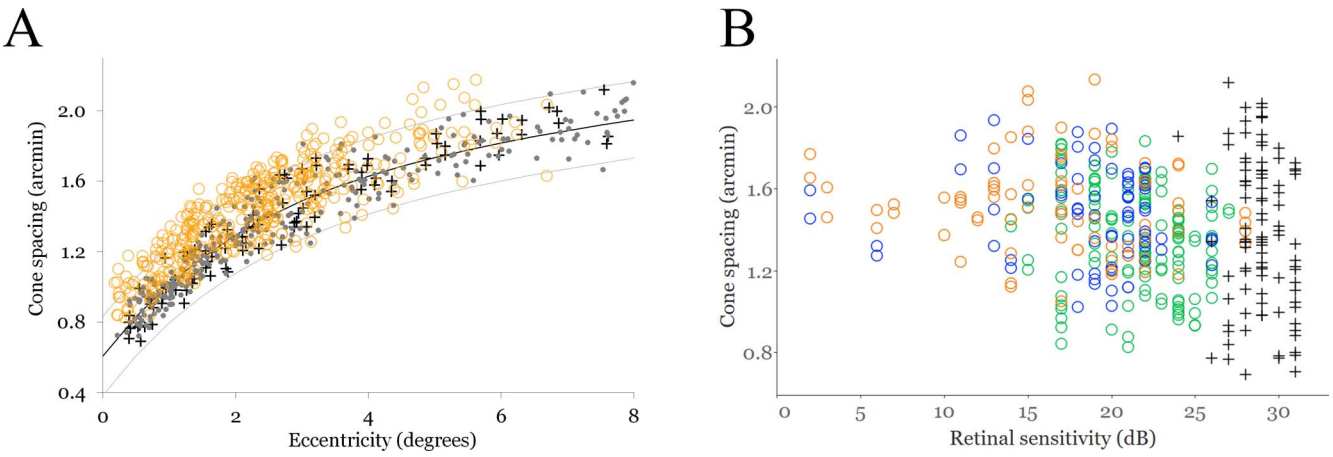

Figure 3. Relationship between cone spacing, eccentricity and retinal sensitivity. **(A)** Cone spacing increased with eccentricity relative to the fovea in patients and normal subjects. The *small gray filled circles* represent a normative dataset composed of 27 healthy controls.[63] The *dotted curved lines* represent the 95% CI of this normative dataset; the *solid black line* represents the mean. Normal subjects from the current study are shown as *black* crosses; patients as *orange circles*. **(B)** Cone spacing was negatively correlated with retinal sensitivity. Normal subjects are shown as *black crosses*, patients are *circles*. Measures that are more than –2° (R1 on Fig. 2A and 2B) within the SS-OCT border are indicated by *green circles*; measures from –2° to –1° within the border are indicated by *blue circles*; measures from –1° to 0° within the border are indicated by *orange circles*.

the present study, cone spacing was significantly correlated with eccentricity for patients ($\rho = 0.89$; 95% CI, 0.79 to 0.95) and normal subjects ($\rho = 0.97$; 95% CI, 0.95 to 0.99; Fig. 3A). To evaluate the relationship between cone spacing and visual function at the same locations where cones were measured, we compared cone spacing with retinal sensitivity and found a significant, negative correlation for patients ($\rho = -0.29$; 95% CI, –0.40 to –0.07) and normal subjects ($\rho = -0.15$; 95% CI, –0.44 to –0.009; Fig. 3B).

We hypothesized that reduced CC perfusion was correlated with outer retinal atrophy. In this study, mean CC flow void was significantly increased in regions approaching and extending beyond the borders of preserved RPE, by either SS-OCT or SW-AF borders (SS-OCT: $\rho = 0.87$; 95% CI, 0.84 to 0.89; SW-AF: $\rho = 0.85$; 95% CI, 0.80 to 0.89; Fig. 4A). Cone spacing expressed as Z-scores was not correlated with distance from the SW-AF or SS-OCT borders (SS-OCT: $\rho = -0.06$; 95% CI, –0.51 to 0.17; SW-AF: $\rho = -0.04$; 95% CI, –0.38 to 0.17; Fig. 4B). There were regions with visible cone IS and OS where cone spacing was measurable that were outside the SW-AF border (Fig. 4B, blue box at +1°, and Figs. 2D, 2E), but no cones were ever evident beyond the SS-OCT border. Retinal sensitivity was measurable, but reduced, 1° to 2° beyond the SW-AF and SS-OCT borders (Fig. 4C). Retinal sensitivity and distance to the SW-AF and SS-OCT borders was significantly, negatively correlated for patients (SW-AF: $\rho = -0.89$; 95% CI, –0.91 to –0.87; SS-OCT: $\rho = -0.91$; 95% CI, –0.94 to –0.86; Fig. 4C). Retinal sensitivity was significantly, negatively correlated with percent CC flow void in eyes when either the SW-AF or SS-OCT borders were used to indicate RPE structure in patients (SW-AF: $\rho = -0.79$; 95% CI, –0.92 to –0.71; SS-OCT: $\rho = -0.81$; 95% CI, –0.91 to –0.76; Fig. 4D) but not in normal subjects ($\rho = 0.37$; 95% CI, –0.86 to 1.00).

To examine the relationship between CC perfusion and cone function, we compared CC flow voids with cone spacing expressed as Z-scores and retinal sensitivity at the region cone spacing was measured. Cone spacing was significantly, negatively correlated with percent CC flow voids for patients ($\rho = -0.29$; 95% CI, –0.60 to –0.11; Fig. 4E) but not normal subjects ($\rho = -0.19$; 95% CI, –0.50 to 3.5). Cone spacing expressed as Z-score was negatively correlated with retinal sensitivity for patients ($\rho = -0.35$; 95% CI, –0.54 to –0.18; Fig. 4F) and normal subjects ($\rho = -0.29$; 95% CI, –0.41 to –0.27).

Comparisons of Structure and Function With OCT Photoreceptor Measurements

Outer Segments. We were interested to know if the cone OS length was affected by reduced blood flow through choriocapillaris, but no correlation was found between OS thickness and percent CC flow void in patients ($\rho = -0.15$; 95% CI, –0.42 to 0.22) or normal subjects ($\rho = 0.52$; 95% CI, –0.69 to 0.82; Fig. 5A). OS thickness has been shown in prior work to correlate with retinal sensitivity in normal subjects and patients with retinitis pigmentosa[64]; in the present study, OS thickness was not significantly correlated with retinal sensitivity in CHM patients ($\rho = 0.22$; 95% CI, –0.13 to 0.48) or normal subjects ($\rho = 0.17$; 95% CI, –0.02 to 0.37; Fig. 5B). OS thickness also was not correlated with cone spacing expressed as Z-scores in CHM patients ($\rho = 0.12$; 95% CI, –0.45 to 0.28; Fig. 5C), but did show a significant, negative correlation for normal subjects ($\rho = -0.39$; 95% CI, –0.83 to –0.27).

Inner Segments. We found no significant correlation between IS thickness and % CC FV for patients ($\rho = -0.08$; 95% CI, –0.22 to 0.15) or normal subjects ($\rho = 0.05$; 95% CI, –0.31 to 0.19; Fig. 6A). No correlation was seen for IS thickness versus retinal sensitivity in patients ($\rho = 0.08$; 95% CI, –0.16 to 0.24), but showed a significant positive correlation for normal subjects ($\rho = 0.13$; 95% CI, 0.03 to 0.15; Fig. 6B). IS thickness was not significantly correlated with cone spacing expressed as Z-scores in patients ($\rho = -0.11$; 95% CI, –0.36 to 0.12), but there was a significant, negative correlation among normal subjects ($\rho = -0.42$; 95% CI, –0.70 to –0.20; Fig. 6C).

Discussion

Multimodal imaging demonstrated several findings that shed light on the mechanism of degeneration in patients with CHM.

What Is the Best Way to Measure the Area of Preserved RPE?

The borders of the presumed area of preserved RPE depended on the method used. In our study, the SS-OCT border did not align with the SW-AF border. This is because neither method measured the RPE directly and, therefore, revealed different features of degeneration in eyes with CHM. The results are

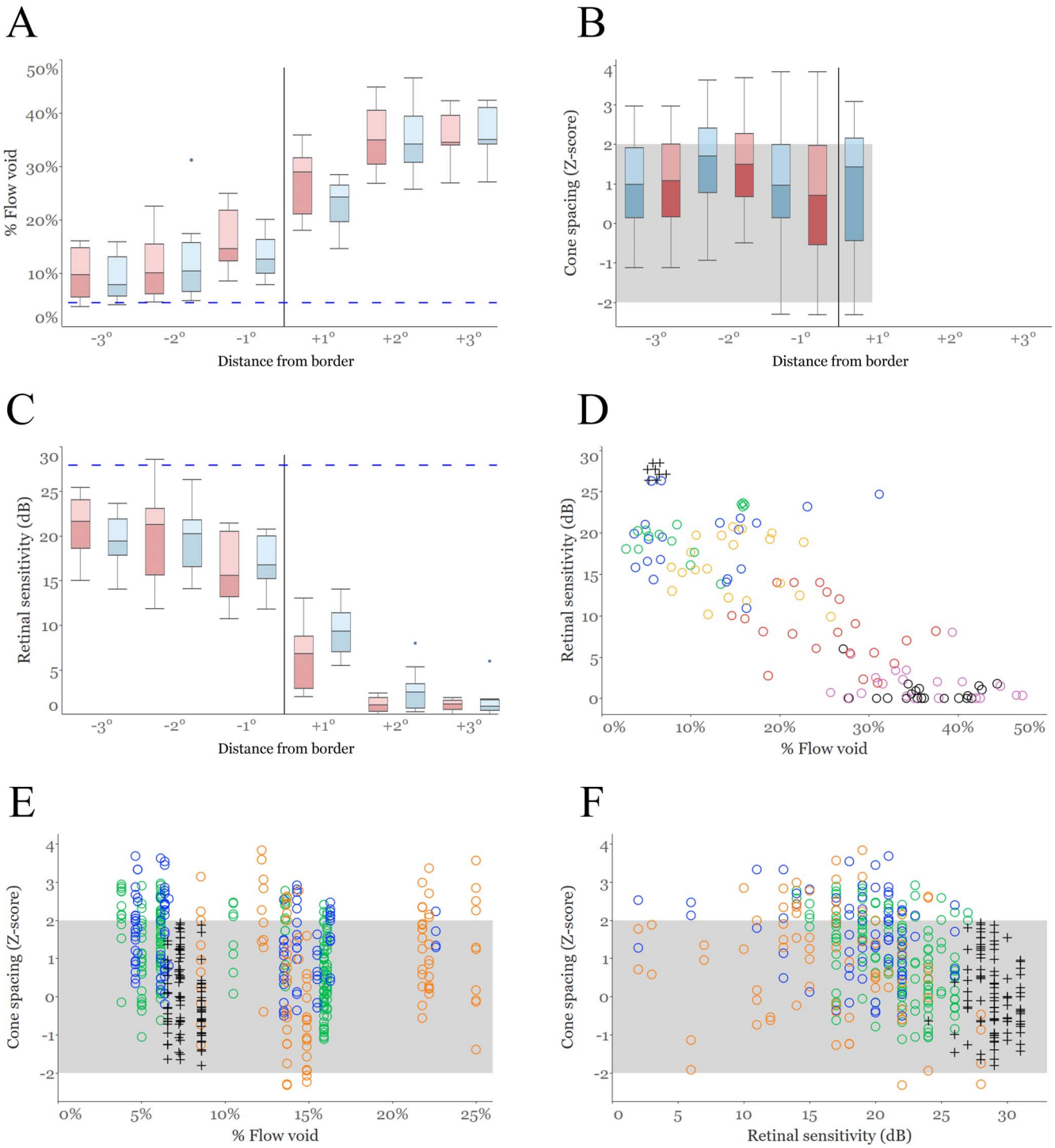

Figure 4. Relationships between flow void, cone spacing, and retinal sensitivity between each other and relative to the SW-AF and SS-OCT borders. Mean CC FV percentages (**A**), cone spacing Z-score (**B**), and mean retinal sensitivity values (**C**) versus distance from the SS-OCT border (*red boxes*) and the SW-AF border (*blue boxes*). The *vertical solid black* line demarcates the border measured by SW-AF and SS-OCT slab. *Horizontal dashed blue lines* indicate normal mean % FV (**A**) and retinal sensitivity (**C**). *Box plots* indicate the middle 50% of the data, which is the middle two quartiles of the distribution, the remaining 50% is represented by *whiskers* displaying all points within 1.5 times the interquartile range. The *gray band* shows the area within which cone spacing measures are normal (**B**). (**D**) Retinal sensitivity versus %FV; (**E**) Cone spacing expressed as Z-score versus %FV; (**F**) Cone spacing expressed as Z-score versus retinal sensitivity. Normal subjects are shown as *black crosses*, patients as *circles*. Measures within −2° of the border are indicated *by green circles*; measures from −2° to −1° inside the border are indicated by *blue circles*; measures from −1° to 0° inside to the border are indicated by *orange circles*; measures from 0° to +1° are indicated by *red circles*; measures from +1° to +2° are indicated by *purple circles*; measures from +2° to +3° are indicated by *black circles*.

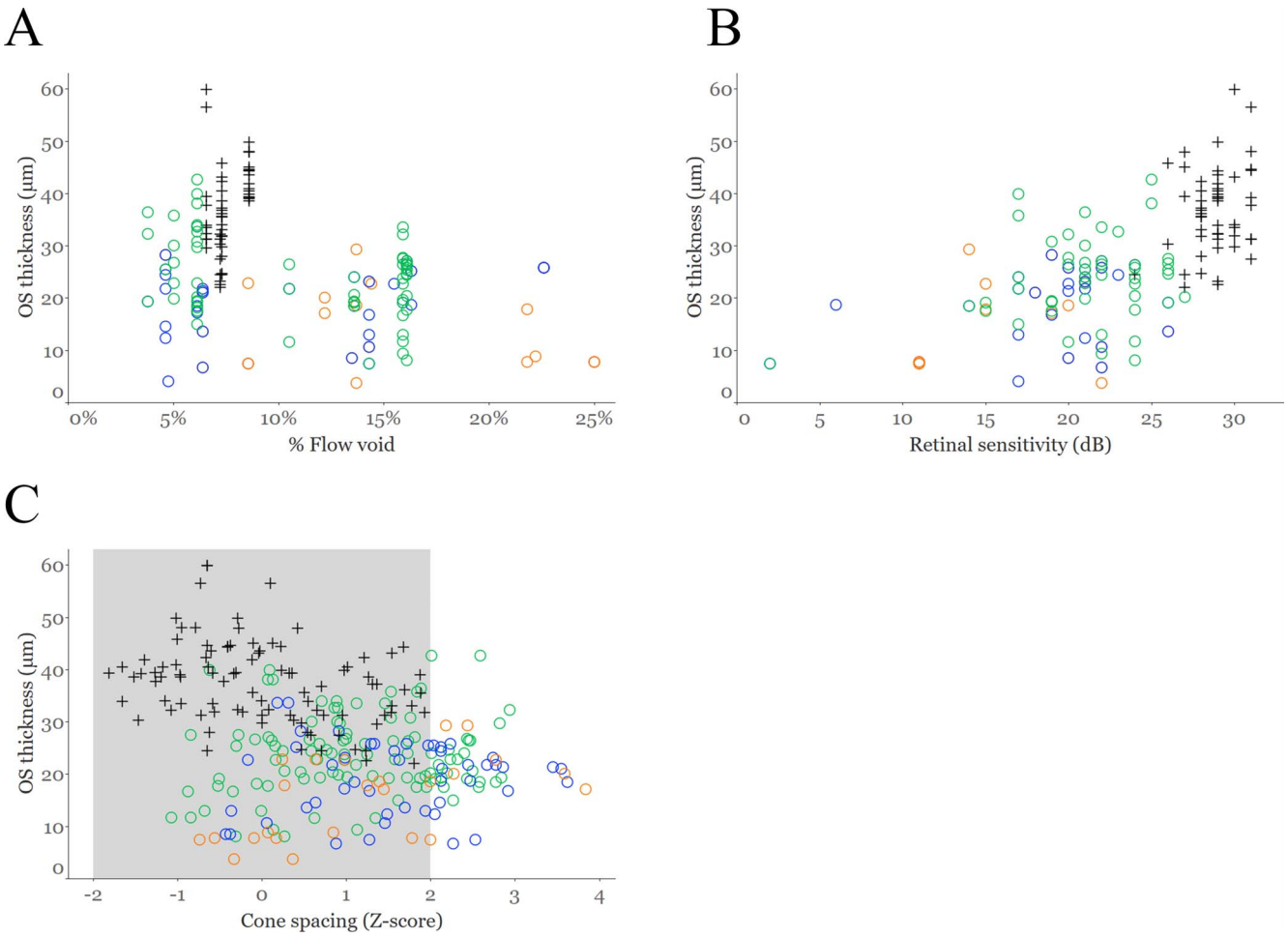

Figure 5. Relationship between OS thickness, %FV, retinal sensitivity, and cone spacing. OS thickness and (**A**) % CC FV; (**B**) retinal sensitivity; (**C**) cone spacing Z-score. Normal subjects are shown as *black crosses*, patients as *circles*. All *graphs* show measures using the SS-OCT-derived outer retina-retinal pigment epithelial-CC slab border. Measures within −2° of the border are indicated by *green circles*; measures from −2° to −1° inside the border are indicated by *blue circles*; and measures from −1° inside to the border are indicated by *orange circles*. The *gray band* shows the Z-score range within which cone spacing measures are normal.

consistent with other studies that found differences comparing separate RPE imaging methods.[36] Discrepancy between NIR-AF and SW-AF also has been reported in patients with Stargardt disease, in which the area of atrophy measured from NIR-AF images was greater than when imaged using SW-AF.[39]

Functional cones were observed beyond the SW-AF border, but not the SS-OCT border (Figs. 2D, 2E). Cone IS and OS were measurable beyond the SW-AF border (Fig. 4B). This agrees with a recent report that the ellipsoid zone (quantified by light scattered in OCT images from the junction between IS and OS in intact cones) extended beyond the borders of the preserved region inferred from SW-AF images in CHM patients.[40] Cone spacing was not correlated with distance from either the SW-AF or SS-OCT borders, indicating cone structure was preserved extending to the edge of atrophy (Fig. 4B).

Retinal sensitivity assessed with fundus-guided microperimetry was lower than normal within the preserved region, and it persisted (albeit significantly reduced) beyond the SW-AF and SS-OCT borders (Fig. 4C). This was not surprising for the SW-AF border, since cones were visualized outside of it, but was unexpected for measurements outside of the SS-OCT border. It is important to note that the stimulus used to assess retinal function with fundus-guided microperimetry (Goldmann III, 26 arcmin, ∼0.43°) was large with respect to the 1° wide bands that were analyzed in this report. The large stimulus size combined with tracking errors may have caused the stimulus to overlap with functioning photoreceptors occasionally. Fundus-guided microperimetry with high-speed fundus tracking and correction of stimulus delivery using AOSLO can refine the precision of stimulus delivery and provide better insight into the structure and function of photoreceptor cells.[21] In a recent study of CHM patients using adaptive optics microperimetry, Tuten et al.[20] found that function was measureable wherever cones were observed in the preserved region (with the exception of cones in outer retinal tubules), and no measureable sensitivity was ever found where cones were not seen. In that study, the border was defined by the visibility of photoreceptors in the AOSLO images.

The cone structures seen extending beyond the SW-AF border suggest cones persist beyond areas with bisretinoid constituents in the OSs and RPE cells. Cone structures beyond the SW-AF border included cone ISs on split detector images, and OSs seen on confocal AOSLO images (Figs. 2D–E), and retinal sensitivity was measurable, although reduced, extending from +1° to +2° beyond the SW-AF border (Figs. 2C, 4C). The results may indicate that the OSs extending beyond the SW-AF border do not contain bisretinoid constituents, but they may be capable of visual function. Measurable retinal sensitivity extending beyond the SW-AF margin (Figs. 2C, 4C) indicates there are OSs and RPE cells in these regions that lack

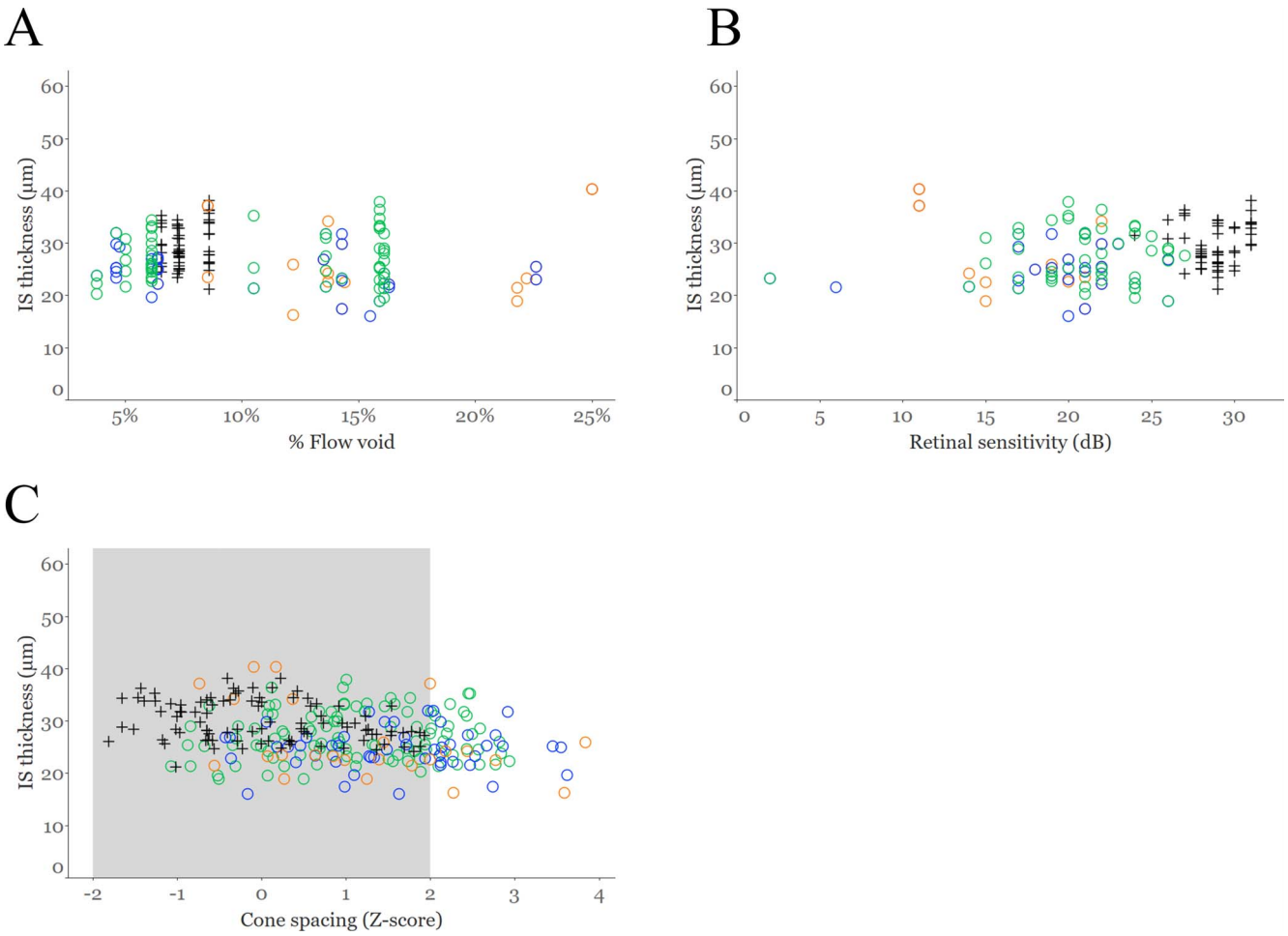

Figure 6. Relationship between IS thickness, %FV, retinal sensitivity, and cone spacing. IS thickness and (**A**) % CC FV; (**B**) retinal sensitivity; (**C**) cone spacing Z-scores. Normal subjects are shown as *black crosses*, patients as *circles*. All graphs show measures using the OCT outer retina-retinal pigment epithelial-CC slab border. Measures within −2° of the border are indicated by *green circles*; measures from −2° to −1° inside the border are indicated by *blue circles*; and measures from −1° inside to the border are indicated by *orange circles*. The *gray band* shows the area within which cone spacing measures are normal.

normal SW-AF, although they demonstrate reduced sensitivity compared to regions located within the SW-AF margin.

Whatever the cause, the persisting functional photoreceptors beyond the presumed borders of RPE inferred by SW-AF may affect clinical trials and evaluations of treatments that target preserved retinal structures based on SW-AF images. Photoreceptors may persist and be amenable to therapy in regions beyond the SW-AF border, and could potentially show improved sensitivity in response to treatments, since the ISs and outer nuclear layer persist in some areas.

Relationships Between RPE and CC Perfusion

Patients with CHM showed abnormal CC perfusion, measured as flow voids, even within regions of preserved outer retinal and RPE structure (Fig. 4A). The results suggested that the CC is unhealthy before the RPE and outer retina degenerates. A range of alterations in CC has been reported in CHM patients[41,42,65] and CC perfusion decreases in conjunction with RPE loss measured by SW-AF.[42] It is possible that cones are more dependent on the CC than the RPE due to the contribution that Muller cells may have on the cone visual cycle, or are less dependent on disc shedding than rods; therefore, requiring less support from the RPE.[66] In patients with CHM, cone spacing correlated negatively with CC flow void and retinal sensitivity. The negative correlation between cone spacing, sensitivity, and flow void suggests that sensitivity was abnormal in areas of reduced CC perfusion. The negative correlation between cone spacing and retinal sensitivity may indicate that cones that are present show reduced function. This is consistent with prior reports suggesting abnormal photoreceptor function precedes RPE loss,[1,44] and also with the observation of visible cone IS and OS with reduced sensitivity extending beyond the margin of RPE as measured by SW-AF in our study.

Relationships Between IS and OS Thickness and Other Structure/Function Measures

OS thickness was not correlated with CC flow void (Fig. 5A), retinal sensitivity (Fig. 5B), or cone spacing (Fig. 5C) in CHM patients. This differs from prior reports demonstrating a correlation between OS thickness and retinal sensitivity in patients with retinitis pigmentosa,[67] perhaps because retinitis pigmentosa often is caused by mutations that are expressed primarily in photoreceptors and degeneration occurs first in the OS, then IS, then ONL.[68] Unlike retinitis pigmentosa, CHM shows early thinning of RPE cells in regions with normal OS thickness,[69] and cone spacing was not correlated with distance from the atrophic border in our study, suggesting OS length

may be preserved despite reduced retinal sensitivity in patients with CHM. In normal subjects OS thickness, IS thickness and cone spacing were negatively correlated (Figs. 5C, 6C), and IS thickness correlated positively with retinal sensitivity (Fig. 6B), likely reflecting greater sensitivities near the fovea where ISs are longest and cone spacing is least in normal eyes. Patients did not show a similar correlation perhaps because in some patients with inherited retinal degeneration cones have abnormal function before they degenerate and lose the ISs, indicating that retinal sensitivity may be a more sensitive measure than cone spacing.

Our study is limited by the small number of patients and the cross-sectional nature of the report. Larger numbers of patients may reveal clearer correlations between photoreceptor, RPE, and CC structure and function. To more clearly understand the mechanism of disease progression, patients will need to be monitored with high resolution retinal imaging approaches, such as those described in our study longitudinally over several years.

Conclusions

The use of multimodal, noninvasive imaging may provide better understanding of the sequence of degeneration in eyes with CHM. Future studies are necessary to examine longitudinal data and degeneration using multimodal techniques, including those used here. While microperimetry can provide a measure of macular sensitivity, AOSLO can visualize photoreceptor morphology. SW-AF as well as SS-OCT can provide information about RPE cells, and SS-OCTA can display CC perfusion. Greater understanding of degeneration and disease progression is crucial to advance the development of novel therapies for this relentless, sight-threatening disease.

Acknowledgments

Supported by National Institutes of Health (NIH; Bethesda, MD, USA) Grants R01EY023591, P30EY002162, R01EY024158, U24EY029891; United States Food and Drug Administration (FDA) Grant R01FD004100; Foundation Fighting Blindness; Research to Prevent Blindness Nelson Trust Award for Retinitis Pigmentosa and Unrestricted Funds; Claire Giannini Foundation; That Man May See, Inc.; NIH Training Grant T32EY007043; Minnie Flaura Turner Memorial Fund for Impaired Vision Research Award; The Bernard A. Newcomb Macular Degeneration Fund; and Hope for Vision.

Disclosure: **K.G. Foote**, None; **N. Rinella**, None; **J. Tang**, None; **N. Bensaid**, None; **H. Zhou**, **Q. Zhang**, P; **R.K. Wang**, P; **T.C. Porco**, None; **A. Roorda**, C. Light Technologies (I), P; **J.L. Duncan**, AGTC (C), ProQR Therapeutics (C), Spark Therapeutics (C), SparingVision (C), 4D Therapeutics (C), Editas Medicine Inc. (C), Biogen (C), Eloxx (C), ProQR Therapeutics (C), Neurotech USA Inc. (F), Allergan (F), NightstaRx (F), Second Sight Medical Products (F)

References

1. Aleman TS, Han G, Serrano LW, et al. Natural history of the central structural abnormalities in choroideremia: a prospective cross-sectional study. *Ophthalmology*. 2017;124:359–373.
2. Coussa RG, Traboulsi EI. Choroideremia: a review of general findings and pathogenesis. *Ophthalmic Genet*. 2012;33:57–65.
3. Duong TT, Vasireddy V, Ramachandran P, et al. Use of induced pluripotent stem cell models to probe the pathogenesis of Choroideremia and to develop a potential treatment. *Stem Cell Res*. 2018;27:140–150.
4. Morgan JI, Han G, Klinman E, et al. High-resolution adaptive optics retinal imaging of cellular structure in choroideremia. *Invest Ophthalmol Vis Sci*. 2014;55:6381–6397.
5. Syed R, Sundquist SM, Ratnam K, et al. High-resolution images of retinal structure in patients with choroideremia. *Invest Ophthalmol Vis Sci*. 2013;54:950–961.
6. Birch DG, Locke KG, Wen Y, Locke KI, Hoffman DR, Hood DC. Spectral-domain optical coherence tomography measures of outer segment layer progression in patients with X-linked retinitis pigmentosa. *JAMA Ophthalmol*. 2013;131:1143–1150.
7. Birch DG, Wen Y, Locke K, Hood DC. Rod sensitivity, cone sensitivity, and photoreceptor layer thickness in retinal degenerative diseases. *Invest Ophthalmol Vis Sci*. 2011;52:7141–7147.
8. Hood DC, Cho J, Raza AS, Dale EA, Wang M. Reliability of a computer-aided manual procedure for segmenting optical coherence tomography scans. *Optom Vis Sci*. 2011;88:113–123.
9. Hood DC, Lazow MA, Locke KG, Greenstein VC, Birch DG. The transition zone between healthy and diseased retina in patients with retinitis pigmentosa. *Invest Ophthalmol Vis Sci*. 2011;52:101–108.
10. Hood DC, Lin CE, Lazow MA, Locke KG, Zhang X, Birch DG. Thickness of receptor and post-receptor retinal layers in patients with retinitis pigmentosa measured with frequency-domain optical coherence tomography. *Invest Ophthalmol Vis Sci*. 2009;50:2328–2336.
11. Wen Y, Klein M, Hood DC, Birch DG. Relationships among multifocal electroretinogram amplitude, visual field sensitivity, and SD-OCT receptor layer thicknesses in patients with retinitis pigmentosa. *Invest Ophthalmol Vis Sci*. 2012;53:833–840.
12. Wen Y, Locke KG, Klein M, et al. Phenotypic characterization of 3 families with autosomal dominant retinitis pigmentosa due to mutations in KLHL7. *Arch Ophthalmol*. 2011;129:1475–1482.
13. Liang J, Williams DR, Miller DT. Supernormal vision and high-resolution retinal imaging through adaptive optics. *J Opt Soc Am A Opt Image Sci Vis*. 1997;14:2884–2892.
14. Zhang Y, Rha J, Jonnal R, Miller D. Adaptive optics parallel spectral domain optical coherence tomography for imaging the living retina. *Opt Express*. 2005;13:4792–4811.
15. Roorda A, Romero-Borja F, Donnelly W III, Queener H, Hebert T, Campbell M. Adaptive optics scanning laser ophthalmoscopy. *Opt Express*. 2002;10:405–412.
16. Duncan JL, Zhang Y, Gandhi J, et al. High-resolution imaging with adaptive optics in patients with inherited retinal degeneration. *Invest Ophthalmol Vis Sci*. 2007;48:3283–3291.
17. Chui TY, Vannasdale DA, Burns SA. The use of forward scatter to improve retinal vascular imaging with an adaptive optics scanning laser ophthalmoscope. *Biomed Opt Express*. 2012;3:2537–2549.
18. Scoles D, Sulai YN, Langlo CS, et al. In vivo imaging of human cone photoreceptor inner segments. *Invest Ophthalmol Vis Sci*. 2014;55:4244–4251.
19. Sun LW, Johnson RD, Williams V, et al. Multimodal imaging of photoreceptor structure in choroideremia. *PLoS One*. 2016;11:e0167526.
20. Tuten WS, Vergilio GK, Young GJ, et al. Visual function at the atrophic border in choroideremia assessed with adaptive optics microperimetry. *Ophthalmol Retina*. 2019;3:888–899.
21. Tuten WS, Tiruveedhula P, Roorda A. Adaptive optics scanning laser ophthalmoscope-based microperimetry. *Optom Vis Sci*. 2012;89:563–574.
22. Wang Q, Tuten WS, Lujan BJ, et al. Adaptive optics microperimetry and OCT images show preserved function

and recovery of cone visibility in macular telangiectasia type 2 retinal lesions. *Invest Ophthalmol Vis Sci*. 2015;56:778–786.

23. Huang Y, Zhang Q, Thorell MR, et al. Swept-source OCT angiography of the retinal vasculature using intensity differentiation-based optical microangiography algorithms. *Ophthalmic Surg Lasers Imaging Retina*. 2014;45:382–389.
24. Podoleanu AG, Rosen RB. Combinations of techniques in imaging the retina with high resolution. *Prog Retin Eye Res*. 2008;27:464–499.
25. Greenstein VC, Nunez J, Lee W, et al. A comparison of en face optical coherence tomography and fundus autofluorescence in Stargardt disease. *Invest Ophthalmol Vis Sci*. 2017;58:5227–5236.
26. Jia Y, Bailey ST, Hwang TS, et al. Quantitative optical coherence tomography angiography of vascular abnormalities in the living human eye. *Proc Natl Acad Sci U S A*. 2015;112:E2395–E2402.
27. Zhang Q, Chen CL, Chu Z, et al. Automated quantitation of choroidal neovascularization: a comparison study between spectral-domain and swept-source OCT angiograms. *Invest Ophthalmol Vis Sci*. 2017;58:1506–1513.
28. Zhang Q, Zheng F, Motulsky EH, et al. A novel strategy for quantifying choriocapillaris flow voids using swept-source OCT angiography. *Invest Ophthalmol Vis Sci*. 2018;59:203–211.
29. Birtel J, Salvetti AP, Jolly JK, et al. Near-infrared autofluorescence in choroideremia: anatomic and functional correlations. *Am J Ophthalmol*. 2019;199:19–27.
30. Sparrow JR, Gregory-Roberts E, Yamamoto K, et al. The bisretinoids of retinal pigment epithelium. *Prog Retin Eye Res*. 2012;31:121–135.
31. Schmitz-Valckenberg S, Holz FG, Bird AC, Spaide RF. Fundus autofluorescence imaging: review and perspectives. *Retina*. 2008;28:385–409.
32. Sparrow JR. Light come shining: fundus autofluorescence. *J Pediatr Ophthalmol Strabismus*. 2018;55:285–286.
33. Weinberger AW, Lappas A, Kirschkamp T, et al. Fundus near infrared fluorescence correlates with fundus near infrared reflectance. *Invest Ophthalmol Vis Sci*. 2006;47:3098–3108.
34. Cideciyan AV, Swider M, Aleman TS, et al. Reduced-illuminance autofluorescence imaging in ABCA4-associated retinal degenerations. *J Opt Soc Am A Opt Image Sci Vis*. 2007;24:1457–1467.
35. Cideciyan AV, Swider M, Jacobson SG. Autofluorescence imaging with near-infrared excitation:normalization by reflectance to reduce signal from choroidal fluorophores. *Invest Ophthalmol Vis Sci*. 2015;56:3393–3406.
36. Paavo M, Carvalho JRL Jr, Lee W, Sengillo JD, Tsang SH, Sparrow JR. Patterns and intensities of near-infrared and short-wavelength fundus autofluorescence in choroideremia probands and carriers. *Invest Ophthalmol Vis Sci*. 2019;60:3752–3761.
37. Fingler J, Schwartz D, Yang C, Fraser SE. Mobility and transverse flow visualization using phase variance contrast with spectral domain optical coherence tomography. *Opt Express*. 2007;15:12636–12653.
38. Schwartz DM, Fingler J, Kim DY, et al. Phase-variance optical coherence tomography: a technique for noninvasive angiography. *Ophthalmology*. 2014;121:180–187.
39. Duncker T, Marsiglia M, Lee W, et al. Correlations among near-infrared and short-wavelength autofluorescence and spectral-domain optical coherence tomography in recessive Stargardt disease. *Invest Ophthalmol Vis Sci*. 2014;55:8134–8143.
40. Hariri AH, Velaga SB, Girach A, et al. Measurement and reproducibility of preserved ellipsoid zone area and preserved retinal pigment epithelium area in eyes with choroideremia. *Am J Ophthalmol*. 2017;179:110–117.
41. Gao SS, Patel RC, Jain N, et al. Choriocapillaris evaluation in choroideremia using optical coherence tomography angiography. *Biomed Opt Express*. 2017;8:48–56.
42. Jain N, Jia Y, Gao SS, et al. Optical coherence tomography angiography in choroideremia: correlating choriocapillaris loss with overlying degeneration. *JAMA Ophthalmol*. 2016;134:697–702.
43. Battaglia Parodi M, Arrigo A, MacLaren RE, et al. Vascular alterations revealed with optical coherence tomography angiography in patients with choroideremia. *Retina*. 2018;187:61–70.
44. Duncan JL, Aleman TS, Gardner LM, et al. Macular pigment and lutein supplementation in choroideremia. *Exp Eye Res*. 2002;74:371–381.
45. Jacobson SG, Cideciyan AV, Sumaroka A, et al. Remodeling of the human retina in choroideremia: rab escort protein 1 (REP-1) mutations. *Invest Ophthalmol Vis Sci*. 2006;47:4113–4120.
46. EyeGENE. National Ophthalmic Disease Genotyping Network. *Insight*. 2009;34:27.
47. Blain D, Goetz KE, Ayyagari R, Tumminia SJ. eyeGENE®: a vision community resource facilitating patient care and paving the path for research through molecular diagnostic testing. *Clin Genet*. 2013;84:190–197.
48. Brooks BP, Macdonald IM, Tumminia SJ, et al. Genomics in the era of molecular ophthalmology: reflections on the National Ophthalmic Disease Genotyping Network (eyeGENE). *Arch Ophthalmol*. 2008;126:424–425.
49. Goetz KE, Reeves MJ, Tumminia SJ, Brooks BP. eyeGENE®: a novel approach to combine clinical testing and researching genetic ocular disease. *Curr Opin Ophthalmol*. 2012;23:355–363.
50. Crossland MD, Jackson ML, Seiple WH. Microperimetry: a review of fundus related perimetry. *Optome Rep*. 2012;2:2.
51. Dimopoulos IS, Tseng C, MacDonald IM. Microperimetry as an outcome measure in choroideremia trials: reproducibility and beyond. *Invest Ophthalmol Vis Sci*. 2016;57:4151–4161.
52. Roorda A, Duncan JL. Adaptive optics ophthalmoscopy. *Annu Rev Vis Sci*. 2015;1:19–50.
53. Dubra A, Sulai Y, Norris JL, et al. Noninvasive imaging of the human rod photoreceptor mosaic using a confocal adaptive optics scanning ophthalmoscope. *Biomed Opt Express*. 2011;2:1864–1876.
54. Chen M, Cooper RF, Han GK, Gee J, Brainard DH, Morgan JI. Multi-modal automatic montaging of adaptive optics retinal images. *Biomed Opt Express*. 2016;7:4899–4918.
55. Poonja S, Patel S, Henry L, Roorda A. Dynamic visual stimulus presentation in an adaptive optics scanning laser ophthalmoscope. *J Refract Surg*. 2005;21:S575–580.
56. Rodieck RW. The density recovery profile: a method for the analysis of points in the plane applicable to retinal studies. *Vis Neurosci*. 1991;6:95–111.
57. Cooper RF, Wilk MA, Tarima S, Carroll J. Evaluating descriptive metrics of the human cone mosaic. *Invest Ophthalmol Vis Sci*. 2016;57:2992–3001.
58. Foote KG, Loumou P, Griffin S, et al. Relationship between foveal cone structure and visual acuity measured with adaptive optics scanning laser ophthalmoscopy in retinal degeneration. *Invest Ophthalmol Vis Sci*. 2018;59:3385–3393.
59. Chui TY, Song H, Burns SA. Adaptive-optics imaging of human cone photoreceptor distribution. *J Opt Soc Am A Opt Image Sci Vis*. 2008;25:3021–3029.
60. Curcio CA, Sloan KR, Kalina RE, Hendrickson AE. Human photoreceptor topography. *J Comp Neurol*. 1990;292:497–523.
61. Elite PLEX 9000 User Manual. *Instructions for Use*. Dublin, CA, USA: Carl Zeiss Meditec; 2016.

Investigative Ophthalmology & Visual Science

62. Akman A. Optical coherence tomography: basics and technical aspects. In: Akman A, Bayer A, Nouri-Mahdavi K, eds. *Optical Coherence Tomography in Glaucoma: A Practical Guide*. Cham, Switzerland: Springer International Publishing AG; 2018:7–12.
63. Chen Y, Ratnam K, Sundquist SM, et al. Cone photoreceptor abnormalities correlate with vision loss in patients with Stargardt disease. *Invest Ophthalmol Vis Sci*. 2011;52:3281–3292.
64. Rangaswamy NV, Patel HM, Locke KG, Hood DC, Birch DG. A comparison of visual field sensitivity to photoreceptor thickness in retinitis pigmentosa. *Invest Ophthalmol Vis Sci*. 2010;51:4213–4219.
65. Kato M, Maruko I, Koizumi H, Iida T. Optical coherence tomography angiography and fundus autofluorescence in the eyes with choroideremia. *BMJ Case Rep*. 2017;2017: bcr2016217682.
66. Wolf G. The visual cycle of the cone photoreceptors of the retina. *Nutr Rev*. 2004;62:283–286.
67. Hariri AH, Zhang HY, Ho A, et al. Quantification of ellipsoid zone changes in retinitis pigmentosa using en face spectral domain-optical coherence tomography. *JAMA Ophthalmol*. 2016;134:628–635.
68. Milam AH, Li ZY, Fariss RN. Histopathology of the human retina in retinitis pigmentosa. *Prog Retin Eye Res*. 1998;17: 175–205.
69. Lazow MA, Hood DC, Ramachandran R, et al. Transition zones between healthy and diseased retina in choroideremia (CHM) and Stargardt disease (STGD) as compared to retinitis pigmentosa (RP). *Invest Ophthalmol Vis Sci*. 2011;52:9581–9590.

Investigative Ophthalmology & Visual Science